Available online at www.sciencedirect.com
SCIENCE DIRECT®
ELSEVIER
Ultramicroscopy 96 (2003) 313–322
ultramicroscopy
www.elsevier.com/locate/ultramic

Localization in elastic and inelastic scattering

A.R. Lupini*, S.J. Pennycook

Solid State Division, Oak Ridge National Laboratory, P.O. Box 2008, Oak Ridge, TN 37831-6031, USA

Received 30 July 2002; accepted 3 November 2002

Abstract

The degree of information localization in elastic and inelastic scattering is examined in the context of imaging zone axis crystals in the aberration corrected STEM. We show that detector geometry is a critical factor in determining the localization, and compare a number of different geometries. Experimental core loss line traces demonstrate strong EELS localization at the titanium L-edge, even in the presence of dynamical elastic scattering.
© 2003 Elsevier Science B.V. All rights reserved.

Keywords: STEM; Aberration; Cs-correction; EELS; Localization; Delocalization; Coherence

1. Introduction

The amount of localization in inelastic scattering is currently of great theoretical interest because it will ultimately determine the attainable resolution in electron energy loss spectroscopy (EELS). This is a source of controversy because semi-classical [1,2] and some quantum mechanical [3,4] calculations predict substantial delocalization, while other quantum mechanical calculations [5–7] give a more localized result.

One reason for this discrepancy is that the simplest semi-classical calculations do not include the transition rate. While an incident electron passing a long distance from the site of interest might still excite a transition, it is less likely to do so than one at a closer range. A weighted average produces a far more localized result [8]. Another reason is that many quantum mechanical calculations that predict delocalization [3,4] invoke the dipole approximation, which replaces $exp\,(\mathbf{iq.r})$ with $1+\mathbf{iq.r}$ in the matrix element. While this is often a reasonable approximation, it will become less accurate as the spatial coordinate, $\mathbf{r}$, and the scattering angle, $\mathbf{q}$, increase [6,9]. Previous calculations suggest that a large or off-axis spectrometer entrance aperture (allowing large $\mathbf{q}$ values) is needed to reduce the size of the inelastic object function [10]. In this case, the dipole approximation will fail to accurately describe the inelastic scattering at longer distances [6].

The precise meaning of localization will depend on the scale being considered. For core-loss spectroscopy, because the important scale is the distance between atomic columns, we will regard an interaction as being localized or delocalized by comparison to the atomic spacings.

Another preliminary consideration is that delocalization has two different but related

*Corresponding author. Condensed Matter Sciences Division, 1 Bethel Valley Road Building 3025, Mailstop 6031, Oak Ridge TN 37923, USA.
E-mail address: gaz@ornl.gov (A.R. Lupini).

0304-3991/03/$ - see front matter © 2003 Elsevier Science B.V. All rights reserved.
doi:10.1016/S0304-3991(03)00096-2

meanings: First, there is the range of the interaction. Does the inelastic interaction take place at significantly larger distances than the elastic interaction? Secondly the probe spreads out as it propagates through the crystal, so some of the probe intensity is "delocalized".

It has already been demonstrated that high angle annular dark field scanning transmission electron microscope (HAADF STEM) images can be directly interpreted at atomic resolution [11]. With the recent advent of aberration correctors [12,13], instrumentation has now advanced to the point where atomic resolution inelastic STEM imaging may be possible. The determining factor will be the localization (or conversely, delocalization) of the inelastic scattering process.

2. Aberration correction and STEM

Aberration correction in STEM is an important development for many reasons [12–15]. However the resolution improvement from aberration correction is more exciting than just another incremental improvement; the resolution of HAADF STEM will cross an important threshold. In an uncorrected system, the probe size, determined by the spherical aberration (C_s), limits the instrumental resolution. However, after the correction of spherical aberration, the probe size can be comparable to the size of the 1s-like Bloch states, and it has been proposed that it will then be the extent of those states that will limit the image resolution [11]. Therefore, as well as providing a useful tool for materials research, an aberration corrector also provides an experimental method for testing the physical resolution limits of the imaging process.

The quadrupole–octupole C_s-corrector fitted to our 100 kV STEM has been described previously [14]. The general principle is that an octupole produces a deflection in the radial direction that can be used to correct the spherical aberration of the objective lens, but has an undesirable 4-fold azimuthal dependence. Thus a series of 4 quadrupoles is used to deform the beam as it passes through 3 octupoles, such that the electron beam leaves the corrector as a round beam with negative spherical aberration. This cancels the unavoidable spherical aberration of the objective lens, and yields an improved resolution and probe current density relative to the uncorrected microscope. As well as improving the image quality, an aberration corrector provides increased resolution and current for EELS analysis, combined with sophisticated computer control [12,14].

We have recently installed an aberration corrector on our 300 kV STEM at ORNL, which is now producing preliminary results. In addition to providing even higher resolution images, this will allow examination of the voltage dependence of the inelastic object function. This has been theoretically shown to be weaker than that predicted by semi-classical calculations [6].

Fig. 1 shows an example HAADF image obtained at 100 kV, from a VG Microscopes' HB501UX STEM fitted with a Nion spherical aberration corrector. This silicon sample has been doped with a low concentration of bismuth atoms. Single atoms of bismuth are visible inside the bulk of the silicon. This image demonstrates the atomic number (Z) dependence [15], the localized nature and single atom sensitivity of the HAADF image. One advantage of the aberration corrector is that we can obtain images of silicon in which the familiar "dumbbells" (spacing 1.36 Å) are visible below the knock-on damage threshold of silicon, demonstrating a significant resolution improvement relative to the uncorrected case.

The principles of STEM operation are schematically illustrated in Fig. 2, and discussed in more detail below. One advantage of STEM when compared to conventional TEM is that the area of the specimen illuminated at one time is smaller, so it would appear possible to obtain more localized information in both images and EEL spectra. Therefore, to calculate how localized the information in an EEL spectrum really is, it is necessary to understand the degree of localization in the inelastic scattering process.

3. Probe delocalization

We can calculate how the probe spreads out as it propagates through the sample by means of a multislice calculation [16]. Unfortunately for

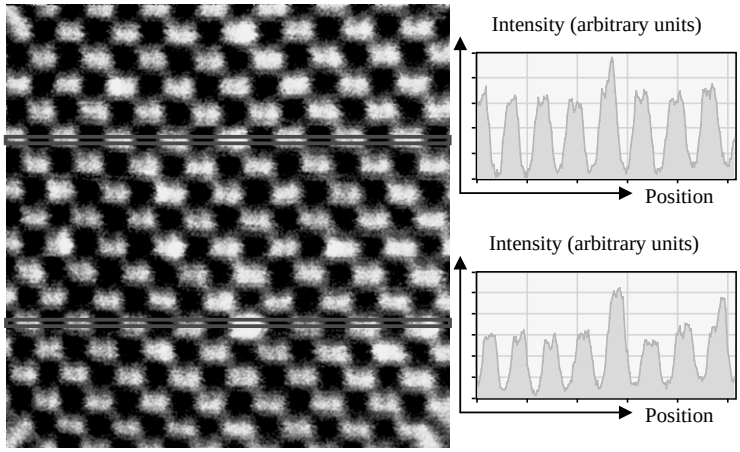

Fig. 1. Example HAADF image obtained with the aberration corrected VG HB501UX STEM (raw data). Silicon [1 1 0] doped with bismuth. Single atoms implanted in the bulk of the silicon wafer are visible. The dumbbell structure is just resolved. Two example line traces of the intensity are shown. Surface damage is also visible, but this has a different appearance to the single atoms.

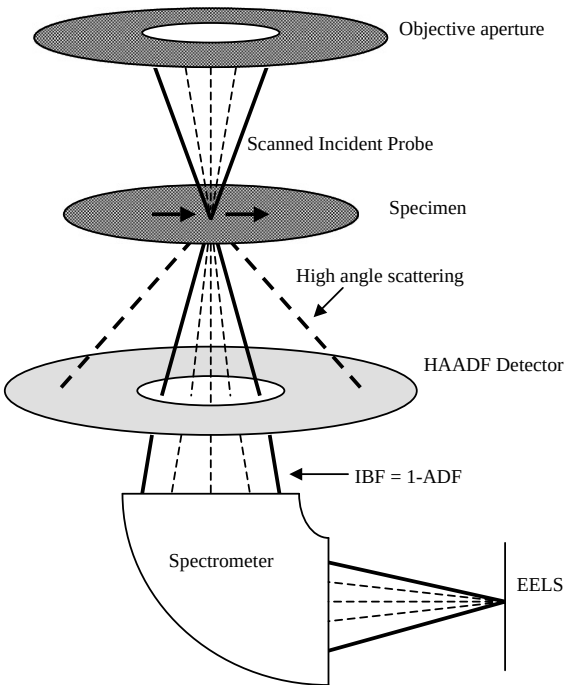

Fig. 2. Schematic of STEM operation with simultaneous EELS acquisition. The probe is scanned across the sample, the intensity scattered to high angles is detected by an ADF detector, and (in principle) all of the intensity passing through the HAADF detector enters the prism, which forms the EEL spectrum.

HAADF STEM images, multislice calculations are computationally expensive, because the entire calculation has to be repeated for every single image point. This is compounded in the frozen phonon model, where the calculation is repeated over many different atomic configurations [17]. It is common to reduce the computation time by calculating a linescan [18]. Similarly, in order to demonstrate the delocalization of the probe due to scattering and channeling effects, the intensity distribution of the probe inside the crystal is often plotted [18–20]. However, this can be misleading because the intensity distribution in the crystal is not directly observable. The relevant factor for image formation is the distribution of the electrons that actually contribute to the image. Clearly this has to depend on the detector and the phase of the wave function.

We now attempt to calculate this intensity distribution. For a scanned image, at any particular point, the image intensity is given by the integration of the electron intensity incident on the detector. So for a detector function, $D(\mathbf{K})$, subtending a range of scattering angles, $\mathbf{K}$, the image intensity, $I(\mathbf{R}_0)$, at a particular probe position, $\mathbf{R}_0$, is given by

$$I(\mathbf{R}_0) = \int D(\mathbf{K})\Psi(\mathbf{K},\mathbf{R}_0)\Psi^*(\mathbf{K},\mathbf{R}_0)\,\mathrm{d}\mathbf{K}, \qquad (1)$$

where $\Psi(\mathbf{K},\mathbf{R}_0)$ is the exit wave function, expressed in reciprocal space, which can be calculated by any method, for example Bloch wave or multislice calculations.

The quantity we are attempting to visualize is the electron intensity weighted by the amount it will contribute to the image, so we will express Eq. (1) entirely in real space. Because the detector function is real and only takes the values 0 or 1, we can write the detector function, $D(\mathbf{K})$, as $D(\mathbf{K})D^*(\mathbf{K})$, to give

$$I(\mathbf{R}_0) = \int D(\mathbf{K})\Psi(\mathbf{K},\mathbf{R}_0)D^*(\mathbf{K})\Psi^*(\mathbf{K},\mathbf{R}_0)\mathrm{d}\mathbf{K}. \quad (2)$$

The reason for this substitution is that we can now use Parseval's theorem, which states

$$\int |Y(\mathbf{K})|^2\,\mathrm{d}\mathbf{K} = \int |y(\mathbf{R})|^2\,\mathrm{d}\mathbf{R}, \quad (3)$$

where $Y(\mathbf{K})$is the Fourier transform of some function, $y(\mathbf{R})$. Therefore the image intensity can be expressed in real space as

$$I(\mathbf{R}_0) = \int \left| \int \psi(\mathbf{R}_1,\mathbf{R}_0)\mathrm{d}(\mathbf{R}-\mathbf{R}_1)\,\mathrm{d}\mathbf{R}_1 \right|^2 \mathrm{d}\mathbf{R}, \quad (4)$$

where $\psi(\mathbf{R},\mathbf{R}_0)$ is the exit wave function in real space (the Fourier transform of the reciprocal space wave function), and $\mathrm{d}(\mathbf{R})$ is the Fourier transform of the detector function

$$\mathrm{d}(\mathbf{R}) = \int D(\mathbf{K})\mathrm{e}^{-2\pi\mathrm{i}\mathbf{K}.\mathbf{R}}\,\mathrm{d}\mathbf{K}. \quad (5)$$

This form is informative because it allows us to demonstrate the effect of the detector in real space. Clearly, as the detector size increases, the real space detector function, $\mathrm{d}(\mathbf{R})$, becomes more localized. Therefore by changing the detector shape, we influence the weight with which different parts of the exit wave function contribute to the observed intensity. Thus it is not the electron intensity in the exit wave function, $|\psi(\mathbf{R},\mathbf{R}_0)|^2$, which is integrated to generate the image intensity for each probe position, $\mathbf{R}_0$. Instead we integrate the intensity $I'(\mathbf{R},\mathbf{R}_0)$, given by

$$I'(\mathbf{R},\mathbf{R}_0) = \left| \int \psi(\mathbf{R}_1,\mathbf{R}_0)\,\mathrm{d}(\mathbf{R}-\mathbf{R}_1)\,\mathrm{d}\mathbf{R}_1 \right|^2 \quad (6)$$

which is the intensity of the convolution of the exit wave function $\psi(\mathbf{R},\mathbf{R}_0)$ with the detector function, $\mathrm{d}(\mathbf{R})$, in real space. Therefore the intensity distribution from Eq. (6) is likely to give a better indication of the effect of probe spreading on the resolution than just considering the intensity of the exit wave function, neglecting the detector.

We can now examine the form of the detector function and its effect for different sorts of detector.

In the limit of an infinitesimally small axial bright field detector, the detector function in reciprocal space is a delta function. Thus $D(\mathbf{K}) = \partial(\mathbf{K})$, implying that it is a constant in real space, $\mathrm{d}(\mathbf{R}) = 1$, giving the image as

$$I(\mathbf{R}_0) = \left| \int \psi(\mathbf{R},\mathbf{R}_0)\,\mathrm{d}\mathbf{R} \right|^2. \quad (7)$$

Eq. (7) displays the well-known phase problem, where the amplitudes interfere and then the intensity is recorded, making it difficult to recover information about the object. Because the detector function in real space is a constant, all parts of the exit wave function contribute with equal weight to the intensity recorded by the detector. In this case, the detector does not provide additional localization to the signal. This is consistent with the delocalized image features sometimes seen in bright-field images.

We can consider the limit in which all electrons are detected. Then the detector function is a constant over all angles, $D(\mathbf{K}) = 1$, implying that it is a delta function in real space, $\mathrm{d}(\mathbf{R}) = \partial(\mathbf{R})$, giving the image intensity in real space as

$$I(\mathbf{R}_0) = \int |\psi(\mathbf{R},\mathbf{R}_0)|^2\,\mathrm{d}\mathbf{R}. \quad (8)$$

Here it is the intensity $|\psi(\mathbf{R},\mathbf{R}_0)|^2$ that is being integrated. Thus the intensity distribution is only really a relevant quantity in the case that we are collecting all of the electrons. However, because of the conservation of energy, this would give no image and only measures the total absorption by the sample. This means in practice that the exit face intensity is not an observable in an electron microscope.

Next consider a high angle ADF detector. This detector, $D(\mathbf{K})$, can be modeled as an infinite detector with a hole in the middle, $H(\mathbf{K})$. Thus $D(\mathbf{K}) = 1 - H(\mathbf{K})$, implying that in real space the

detector function is

$$\mathrm{d}(\mathbf{R}) = \partial(\mathbf{R}) - \frac{2J_1(2\pi u_{\mathrm{in}}|\mathbf{R}|)}{2\pi u_{\mathrm{in}}|\mathbf{R}|}, \tag{9}$$

where $u_{\mathrm{in}} = \theta_{\mathrm{in}}/\lambda$, for inner detector half-angle θ_{in} and electron wavelength λ.

This is optically conjugate to the large angle incoherent bright field (IBF) detector, which collects the intensity admitted through the hole in the middle of the HAADF detector. The width of the Bessel function is inversely related to the aperture size, with the first zero at a radius $0.61\lambda/\theta_{\mathrm{in}}$. Thus as the size of the HAADF (or IBF) detector increases, the localization of the real space detector function, $\mathrm{d}(\mathbf{R})$, increases.

This result is closely related to the coherence envelope in TEM, where the amount of coherence is inversely related to the illumination angle [21]. There too, the coherence is really a measure of how large an area contributes coherently to the image at each point. Essentially the same result applies here; the image coherence or incoherence depends significantly on the size of the detector.

Another interpretation of this result is that the detector function acts as a filter, which can cause much of the intensity distribution in the exit wave function to give very little contribution to the image for a specific probe position. Alternatively, in reciprocal space, it is clear that the high angle detector will be heavily biased towards those electrons that are scattered to high angles. Discussion of a similar result, derived for the specific case of Bloch states is given in Ref. [11]. Equivalently, if we could consider electrons to be discrete particles, then it would be very clear that detectors subtending different angular ranges would in fact collect different electrons, which could have interacted differently and with different volumes of the sample. So it should be no surprise that we see very different images with different detectors.

Fig. 3 shows the output from an example multislice calculation, using the code described in Ref. [16]. The 100 kV STEM probe is incident on one of the "dumbbell" columns in silicon [1 1 0]. The intensity distribution is shown in both real and reciprocal space. However, we must include the detector function to determine how significant the apparent spreading of the probe is. Fig. 4 shows the form of the detector function in real space for different detectors and the intensity distribution, from Eq. (6), for each of those detectors. With a small bright field detector, convolution of the broad real space detector function with the exit face wave function leads to significant delocalization, even though only elastic scattering is considered. As the detector size is increased, the Fourier transform becomes sharper and the structure of the exit face wave function becomes better preserved, although we do see some sensitivity to the adjacent column in the dumbbell. The optically conjugate ADF detector is more localized, and the localization increases with

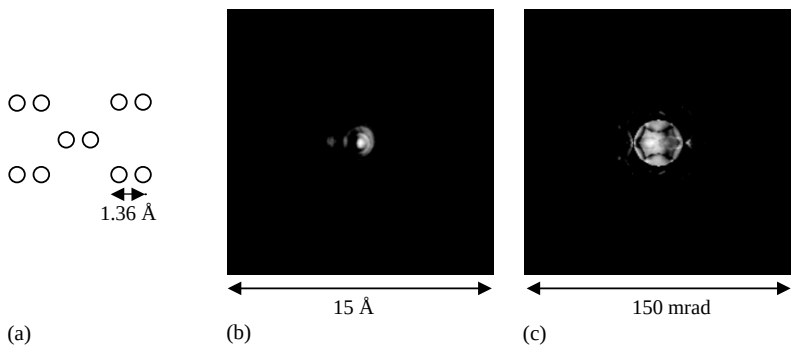

Fig. 3. Output from a multislice calculation, for the example case of silicon [1 1 0] with the probe incident on one of the "dumbbell" columns. (a) Schematic of the "dumbbell" positions. The intensity distribution of the exit wave function is shown in (b) real, and (c) reciprocal space. Parameters used were for a lens with $C_s = 0.5$ mm, with defocus of -430 nm and aperture half angle 13.3 mrad, for 76.8 Å thickness. 10 phonon configurations were used with the temperature set to 300 K, but chromatic aberration was not included.

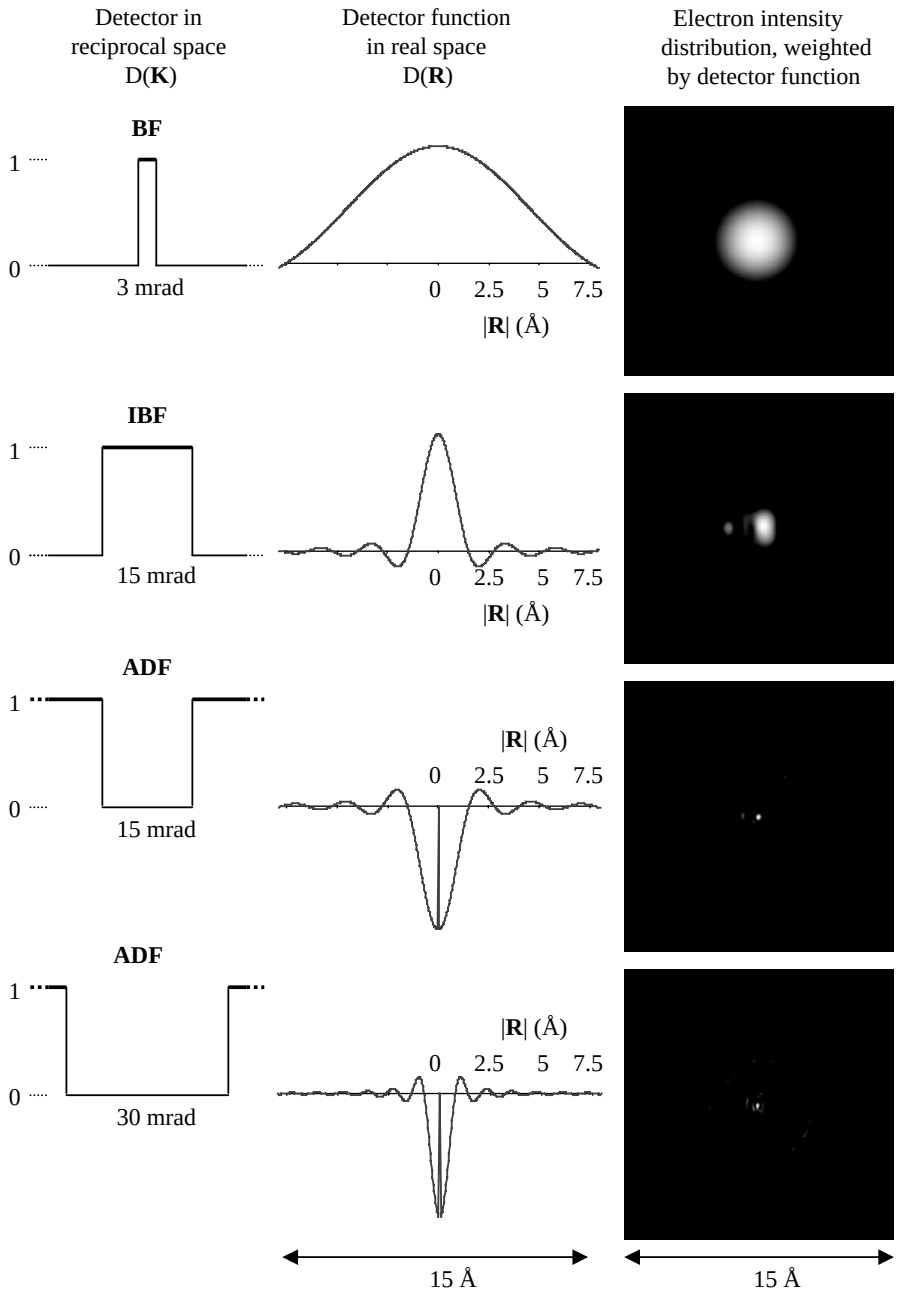

Fig. 4. Example detectors (with angular radius shown), their detector functions in real space, and intensity distributions weighted by their contribution to the image shown in real space. The intensity distributions, from Eq. (6), are each normalized independently, because of the variation in intensities. The same parameters and exit wave function from Fig. 3 were used.

increasing inner detector angle. Experimentally it is also important that increasing the inner angle of the ADF detector will reduce the available intensity. If the probe is positioned between the columns, we still see significant probe spreading as reported by Dwyer and Etheridge [20]. However,

for the case of a HAADF image of an aligned crystal, we suggest that this, and the probe "tails" evident in Fig. 4, will in fact just contribute an almost uniform background to the overall image intensity. This effect would be important in some cases, such as when measuring a concentration gradient across an interface.

Finally, we observe that the localization or delocalization provided by the detector acts on the exit wave function, so to achieve an atomically resolved incoherent image, a suitable probe and specimen remain necessary.

4. A simple incoherent model for comparing elastic and inelastic scattering

The HAADF image can be described extremely well by an incoherent model [15]. In an incoherent image, the intensity is given by the convolution between a resolution function (the effective probe, $P^2_{\mathrm{Eff}}(\mathbf{R})$), and an object function, $O(\mathbf{R})$:

$$I_{\mathrm{ADF}}(\mathbf{R}) = O(\mathbf{R}) \otimes P^2_{\mathrm{Eff}}(\mathbf{R}). \tag{10}$$

For the object function it is convenient to use an array of delta functions at the column positions, $\partial(\mathbf{R})$. This form is computationally simple to handle and gives a very good match to experimental images. There are some discrepancies, such as the systematic absence of the (2 0 0) spots in Si[1 1 0], which are normally weakly present experimentally. This arises because the delta function is not really an accurate approximation to the object function, especially for thicker specimens where dynamic effects are important. Using a more suitable function would eliminate the systematic absences, demonstrating that the convolution model is still valid.

This model for incoherent imaging should not be interpreted as representing the probe propagation inside the crystal; it is a description of the final image. There will also be a strong thickness dependence, which we neglect here.

For simplicity, we normalize the total intensity and assume that the HAADF detector extends to infinity. Following on from the previous section, we are able to obtain incoherent imaging conditions by using a large inner angle. For an incoherent bright field detector, collecting the entire signal that passes through the hole in the ADF detector, the image intensity is therefore

$$I_{\mathrm{IBF}}(\mathbf{R}) = 1 - I_{\mathrm{ADF}}(\mathbf{R}). \tag{11}$$

Without accounting for elastic scattering, under incoherent conditions, the total EELS signal for a particular edge can be represented as a convolution between the effective probe and the inelastic object function, $O'(\mathbf{R})$:

$$I_{\mathrm{Edge}}(\mathbf{R}) = O'(\mathbf{R}) \otimes P^2_{\mathrm{Eff}}(\mathbf{R}). \tag{12}$$

Elastic scattering (to the ADF detector) reduces the intensity that passes into the spectrometer, so it is reasonable to assume that the measured signal for that edge in the EELS image will be modulated by the total incoherent bright field intensity:

$$I_{\mathrm{EELS}}(\mathbf{R}) = I_{\mathrm{Edge}}(\mathbf{R}) I_{\mathrm{IBF}}(\mathbf{R}). \tag{13}$$

We are now able to consider the 2 limits for the object function, fully localized and fully delocalized.

If the inelastic interaction is fully localized, then in analogy with the HAADF imaging process, we can approximate the inelastic object function as a series of delta functions at the atomic column locations:

$$O'(\mathbf{R}) = \partial(\mathbf{R}). \tag{14}$$

In this case, the EELS image, $I_{\mathrm{EELS}}(\mathbf{R})$, will be given by

$$I_{\mathrm{EELS}}(\mathbf{R}) = \left[\partial(\mathbf{R}) \otimes P^2_{\mathrm{Eff}}(\mathbf{R})\right] \times \left[1 - O(\mathbf{R}) \otimes P^2_{\mathrm{Eff}}(\mathbf{R})\right]. \tag{15}$$

The term in the first set of brackets will resemble the HAADF image with maxima at the atomic column locations. This is modulated by the terms in the second set of brackets, which represent the total intensity entering the spectrometer. Thus we expect the maximum intensity to be at the atomic column locations, although it may be necessary to divide by the total intensity entering the spectrometer for this to be clear.

If the inelastic interaction is fully delocalized (which is to say that the delocalization is significantly bigger than the atomic spacings) then the inelastic object function will become approximately

constant:

$$O'(\mathbf{R}) = 1. \tag{16}$$

In other words, it does not matter exactly where the incident beam passes through the sample in relation to the atomic column position. This gives the EELS signal as

$$I_{\mathrm{EELS}}(\mathbf{R}) = P^2_{\mathrm{Eff}}(\mathbf{R})\left[1 - O(\mathbf{R}) \otimes P^2_{\mathrm{Eff}}(\mathbf{R})\right]. \tag{17}$$

Therefore in this case, the EELS image will resemble the incoherent bright field image. The maximum intensity will lie between the atomic column positions.

Thus it has been shown that the two limits, of full localization and complete delocalization will give very different EELS images of a crystalline structure. For complete delocalization, the maximum EELS signal would be observed between atomic columns, because the modulation due to the elastic scattering would dominate the EELS intensity. However, for a fully localized signal, the maxima will correspond to the atomic column positions. Although the increased high-angle scattering reduces the available intensity, the localization of the interaction outweighs this.

5. An experimental test

Having developed a simple model for incoherent inelastic imaging, we can test the localization experimentally. Theoretical calculations suggest that the inelastic object function for core-loss spectroscopy is localized with a size determined by the geometric extent of the core electron orbital [6]. Therefore experimentally, for incoherent conditions, we would expect the EELS signal to peak on the atomic column positions.

The preceding discussion has shown that in order to obtain a localized signal, it is essential to use a large collection angle. This is important, because early attempts to perform this experiment seemed to suggest significant delocalization: In general for thin specimens, the zero loss, which was taken to represent the IBF image, was often found to behave as the optical conjugate of the HAADF image. However, the core loss signals were also found to vary with the IBF intensity in the same way, consistent with Eq. (17) for a delocalized object function. This is because in its normal configuration, the EEL spectrometer entrance angle is primarily chosen as a compromise between energy resolution and signal intensity, and is far smaller than the inner angle of the HAADF detector. In this case therefore the apparent delocalization is mostly caused by the difference in aperture size, and cannot be taken as an indication that the underlying interaction is significantly more delocalized. Similarly even if the excitation is highly localized, as for example with a very high energy loss, dynamical scattering on the way to the detector can also lead to apparent delocalization.

Experimentally, we used a 2.5 mm collector aperture and a quadrupole coupling module from Nion Co. to provide increased angular compression. Because of the high angles necessary, it was not possible to totally correct the spectrometer aberrations, resulting in a degraded energy resolution. A suitable test sample was found to be strontium titanate. This has a relatively large lattice spacing, several strong edges are available for analysis, and the different atomic columns are readily identified using Z-contrast imaging [15].

Fig. 5 shows the results of a linescan across 2 columns each of titanium and strontium. In this example we used the integrated intensity under the titanium edge in order to obtain an adequate signal-to-noise ratio during the time for which the sample was stable. The integrated HAADF and titanium edge intensities are shown. The background has been subtracted from the titanium intensity, using a least-squares fit, and the result was not found to be particularly sensitive to different background fitting procedures. The maxima in the titanium signal were found to correspond to the positions of the titanium columns identified from the HAADF image. This is consistent with Eq. (15) for a localized object function. This was seen consistently provided the linescan went accurately over the atomic column positions, the sample was thin, and the collection angle was large enough. The contrast variation is not due to elastic contrast because that would cause the edge intensity to peak at the points of maximum intensity in the IBF image, between the columns. Similarly, the edge would then also be

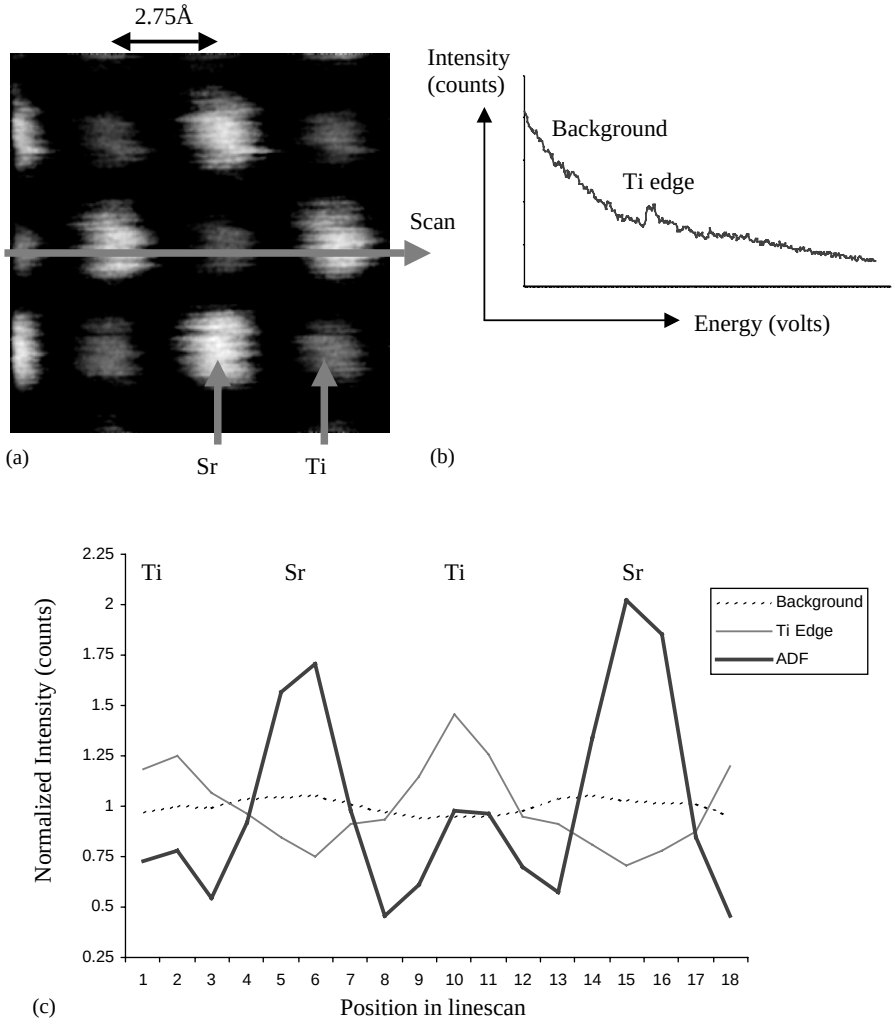

Fig. 5. (a) HAADF STEM image of $SrTiO_3$ taken at 100 kV. Some instabilities are visible. (b) Example of spectra from linescan. Because of the large collection angle, the energy resolution is degraded, and some noise is visible from the short acquisition time. (c) Linescan across strontium and titanium columns. The HAADF, fitted background and integrated titanium edge intensities are shown. Each signal has been normalized to its average value. The titanium edge peaks at the titanium column positions and the background varies more weakly, but peaks at the strontium column positions.

expected to vary in the same manner as the background, which is not seen here.

It was originally intended to obtain the incoherent bright field image by extrapolation from the pre-edge background, as it was difficult to record the zero loss peak simultaneously on our detector because of the huge difference in intensity. However, as is shown in Fig. 5, this did not work for the strontium titanate sample. The probable reason for this failure is that the strontium has several M edges, which increase the background under the titanium L edges, and so the background had maxima at the strontium column positions. Again however, that would be consistent with the result of Eq. (15) for a localized inelastic interaction. Thus we had to take the IBF signal as being the optical conjugate of the HAADF signal (which we normally found to be true with a large entrance

aperture). However, we did not do the division suggested above, because this was extremely sensitive to the black level settings.

The contrast does not go to zero between the columns, because of the amorphous surface layer from the thinning, and instabilities over the acquisition time that cause an effective broadening of the probe. However, what is important is that it was possible to measure a difference in the EEL spectra between different atomic columns that was significantly above the noise level.

The titanium signal was peaked at the titanium columns, and the background, which contained the strontium signal, peaked on the strontium columns. In conclusion therefore, the experimental results were consistent with a localized interaction provided the collection angle was large enough, and the specimen thin.

6. Conclusions

To understand the properties of many materials, particularly at grain boundaries or dopant sites, it is essential to be able to probe the electronic structure with atomic resolution. The higher resolution and increased current density provided by the correction of spherical aberration mean that an aberration corrector will provide an indispensable tool for column by column analysis of such materials. We have shown that representing the detector function in real space provides an indication of the amount of localization for the detectors used in various imaging modes. It is therefore essential to include the detector to draw any meaningful conclusions when interpreting image calculations. Axial bright field imaging is significantly delocalized, even when only elastic scattering is involved. Incoherent bright field and dark field imaging is much more localized.

We have proposed a very simple incoherent model for the image produced by inelastic scattering. Like the incoherent model for elastic scattering, this applies for thin samples, if the detector is large enough. We have presented some experimental results, which demonstrate that the inelastic scattering process is strongly localized. In conclusion then, under incoherent conditions, with a large enough collection aperture, atomic resolution core loss inelastic signals are attainable even in the presence of dynamical elastic scattering.

Acknowledgements

This research was supported by Oak Ridge National Laboratory, Division of Materials Sciences, US Department of Energy, under contract DE-AC05-00OR22725 managed by UT-Battelle, LLC, and by an appointment to the ORNL Postdoctoral Research Associates Program administered jointly by ORNL and ORISE.

References

[1] A. Howie, J. Microsc.-Oxford 117 (1979) 11.
[2] A.J. Bourdillon, P.G. Self, W.M. Stobbs, Philos. Mag. A44 (1981) 1335.
[3] H. Kohl, H. Rose, Adv. Electron. Electron. Phys. 65 (1985) 173.
[4] D.A. Muller, J. Silcox, Ultramicroscopy 59 (1995) 195.
[5] O.F. Holbrook, D.M. Bird, Electron Microsc. Anal. 147 (1995) 175.
[6] B. Rafferty, S.J. Pennycook, Ultramicroscopy 78 (1999) 141.
[7] M.P. Oxley, L.J. Allen, Phys. Rev. B 57 (2000) 3273.
[8] S.J. Pennycook, Ultramicroscopy 26 (1988) 239.
[9] D.W. Essex, P.D. Nellist, C.T. Whelan, Ultramicroscopy 80 (1999) 183.
[10] R.H. Ritchie, A. Howie, Philos. Mag. A 58 (1995) 195.
[11] P.D. Nellist, S.J. Pennycook, Ultramicroscopy 78 (1999) 111.
[12] N. Dellby, O.L. Krivanek, P.D. Nellist, P.E. Batson, A.R. Lupini, J. Electron Microsc. 50 (3) (2001) 177.
[13] M. Haider, S. Uhlemann, E. Schwan, H. Rose, B. Kabius, K. Urban, Nature 392 (1998) 768.
[14] O.L. Krivanek, N. Dellby, A.R. Lupini, Ultramicroscopy 78 (1999) 1.
[15] S.J. Pennycook, B. Rafferty, P.D. Nellist, Microsc. Microanal. 6 (2000) 343.
[16] E.J. Kirkland, Advanced Computing in Electron Microscopy, Plenum Press, New York, 1998.
[17] R.F. Loane, P. Xu, J. Silcox, Acta Cryst. A47 (1991) 267.
[18] S. Hillyard, J. Silcox, Ultramicroscopy 58 (1995) 6.
[19] T. Plamann, M.J. Hytch, Ultramicroscopy 78 (1999) 153.
[20] C. Dwyer, J. Etheridge, Inst. Phys. Conf. Series 168 (4) (2001) 127.
[21] J.C.H. Spence, Experimental High-Resolution Electron Microscopy, Oxford University Press, New York, 1998.